Check for updates

Advanced Materials Technologies

ADVANCED MATERIALS TECHNOLOGIES
www.advmattechnol.com

RESEARCH ARTICLE OPEN ACCESS

Laser-Induced Local De-Doping in Organic Semiconductors

Christian Rainer[1,2] | Aleksandr Perevedentsev[1,2,3] | Daniel Ryklin[4] | Rasmus R. Schröder[4] | Gerardo Hernandez-Sosa[1,2,5,6] | Uli Lemmer[1,2,5]

[1]Light Technology Institute, Karlsruhe Institute of Technology (KIT), Karlsruhe, Germany | [2]InnovationLab GmbH, Heidelberg, Germany | [3]Institut de Ciència de Materials de Barcelona (ICMAB-CSIC), Bellaterra, Spain | [4]BioQuant, Heidelberg University, Heidelberg, Germany | [5]Institute of Microstructure Technology, Karlsruhe Institute of Technology (KIT), Eggenstein-Leopoldshafen, Germany | [6]Institute for Automation and Applied Informatics, Karlsruhe Institute of Technology (KIT), Eggenstein-Leopoldshafen, Germany

Correspondence: Uli Lemmer (uli.lemmer@kit.edu)

Received: 1 June 2026 | **Revised:** 5 August 2026 | **Accepted:** 27 August 2026

Keywords: de-doping | laser patterning | laser processing | organic electronics | polymer

ABSTRACT

This study explores control of the doping level in organic semiconductor films using scanning continuous wave laser radiation. The feasibility of this one-step non-contact post-deposition approach is explored for a benchmark material system comprising the high-mobility polymeric semiconductor PBTTT-C14 p-doped with the small-molecular acceptor F_4TCNQ. De-doping is achieved via laser-driven photothermal heating that induces neutralization and subsequent diffusion and/or sublimation of dopant molecules from the irradiated region. Comparison of 785 and 561 nm excitation, which are resonant with the absorption features of doped and neutral semiconductor, respectively, reveals that excitation at 785 nm leads to a less pronounced organic semiconductor degradation at comparable laser irradiance. Modulation of doping level is achieved with laser-resolution-limited feature sizes below 10 µm, with laser power adjustment enabling the tunability of electrical resistance by two and five orders of magnitude for excitation at 785 and 561 nm, respectively. This fully digital process is conducted in ambient atmosphere and does not require any additional equipment, therefore allowing straightforward integration with high-throughput mass-production of molecular electronics.

1 | Introduction

Organic semiconductors represent a highly versatile class of materials, offering numerous possibilities for electronic applications due to their ease of fabrication and cost-effectiveness. Many materials of this class are solution-processable and offer a wide range of electronic properties, enabling their use in various electronic applications. However, semiconducting organic polymers typically lack sufficient intrinsic conductivity and require application-specific engineering. Molecular doping provides a pathway to tailor the electrical performance of these materials by incorporating a dopant molecule into a host polymer matrix, increasing charge-carrier density [1–5]. This is crucial for enabling applications in organic light-emitting diodes (OLEDs) [6, 7], organic photovoltaics (PV) [8, 9], organic field-effect transistors (OFETs) [10–13], and organic thermoelectric generators (OTEGs) [14, 15].

While *macroscopic, spatially-uniform* doping of organic semiconductors with molecular acceptors or donors is commonly achieved at the materials deposition step by solution-based approaches [16–19] or as a post-deposition step using solution- or vapor-phase doping [20, 21], *patterned* doping remains a challenge for the fabrication of molecular electronic devices. A case-in-point is the example of OFETs—the fundamental unit of active electronic circuits—where p-doping with molecular acceptors has become the standard [10]. Minimizing contact resistance via local doping is vital for realizing low-power, high-frequency device operation. Although shadow-masked vapor-phase doping [14, 22] represents the common laboratory-scale approach, the

This is an open access article under the terms of the Creative Commons Attribution License, which permits use, distribution and reproduction in any medium, provided the original work is properly cited.
© 2026 The Author(s). *Advanced Materials Technologies* published by Wiley-VCH GmbH

mask alignment and high-vacuum requirements are a challenge for upscaling. On the other hand, application of conventional ink-based printing to locally dope the organic semiconductor generally does not provide the required high spatial resolution, requiring more sophisticated alternatives [23].

Laser-based approaches to doping patterning offer the key advantages of digital, mask-free, and non-contact fabrication. Previous reports demonstrated a mixed laser/solvent-immersion approach to the fabrication of negative doping patterns (that is, laser-induced de-doping) [24–26]. While enabling the formation of sub-micrometer patterns by dissolution of de-doped material, this approach is inherently batch-type and necessitates subsequent back-filling with the pristine organic semiconductor to obtain the desired spatial patterns of doping. Elsewhere, the solution-sequential 'molecular gate' approach was shown to yield positive doping patterns with 10 μm spatial resolution by local laser-induced dopant diffusion within sacrificial multilayer films, albeit with the additional requirement of subsequent solution-based removal of the auxiliary layers [27].

To address the limitations of the above-described laser-based approaches, we present and investigate a 'dry' process that directly utilizes laser radiation to controllably de-dope organic semiconductor thin films. The method is based on resonant optical excitation, photothermal conversion, and subsequent sublimation of the molecular dopant from the 'baseline' pre-doped semiconductor layers. By managing laser processing parameters, the modulation of the original doping level via de-doping can be carefully controlled. Two parameters are of particular interest: the laser irradiance I_L , expressed in kW cm^{-2}, and the feed-rate v, expressed in mm s^{-1}. The latter corresponds to the linear movement speed of the focused laser beam across the sample surface during processing. We employ two laser sources at 561 and 785 nm wavelengths for processing, and analyze the resulting semiconductor films using UV–vis and Raman spectroscopy, as well as SEM. As the material system, we focus on the benchmark blend comprising the high-mobility semiconducting polymer poly[2,5-bis(3-tetradecylthiophen-2-yl)thieno[3,2-*b*]thiophene] (PBTTT-C14) and the molecular acceptor 2,3,5,6-tetrafluoro-7,7,8,8-tetracyanoquinodimethane (F_4TCNQ). The doping process, thermal stability and characteristics of the resulting films for this material system have been extensively studied in previous reports [22, 28–32]. In particular, F_4TCNQ has been shown to undergo relatively rapid de-doping at a temperature of 100°C in comparison to alternative dopants [28], which further motivates its selection for the present study.

2 | Results and Discussion

2.1 | Process Principle and Parameter Screening

Chemical structures of the materials are depicted in Figure 1a, with the semiconducting polymer PBTTT-C14 hereafter referred to as 'PBTTT'. 160-nm-thick films of PBTTT are deposited onto glass substrates by gas-assisted blade-coating [33] (Figure 1b), followed by thermal annealing and, finally, vapor-phase doping with F_4TCNQ (Figure 1c); see Experimental Section 4.2 for further details. The obtained films correspond to the 'baseline' samples for subsequent laser-based patterning and are hereafter termed 'as-doped'. Neutral, as-deposited films are referred to as 'pristine'.

The de-doping process is enabled by focusing a continuous-wave (cw) laser onto the doped polymer thin film, as schematically depicted in Figure 1d. The laser system is integrated into an industrial inkjet printing platform, and areas used for analysis and characterization are patterned by performing a raster scan. This is achieved by placing laser paths parallel to one another with a controlled overlap between adjacent passes. Each path is referred to as a laser swath, and the center-to-center distance between two neighboring swaths is defined as the interline laser swath spacing, called '*d*'. This parameter determines the degree of overlap between adjacent laser passes and therefore influences the homogeneity of the resulting de-doped area.

In the employed system, the focused laser beam has an approximate theoretical diameter of 12 μm for the 561 nm laser and 15 μm for the 785 nm laser, according to Equation (1):

$$d_f = 2 \cdot \omega_0 = \frac{4M^2}{\pi} \cdot \frac{\lambda F}{D} \tag{1}$$

where d_f is the beam diameter in the focal spot, F is the focal length of the focusing optical lens, λ is the laser wavelength, D is the diameter of the collimated laser beam before the focusing lens, and ω_0 is the beam waist at the focal point. M^2 is a parameter describing the quality of the output beam profile in relation to an ideal Gaussian beam, provided by the laser manufacturer. All parameters are summarized in Table S1. Assuming a Gaussian beam profile, the laser irradiance I_L can therefore be calculated using Equation (2):

$$I_L = \frac{2 \cdot P_{laser}}{\pi \cdot \left(\frac{d_f}{2}\right)^2} \tag{2}$$

where P_{laser} is the incident laser power and d_f the diameter of the focused beam. Irradiance is a property that allows direct comparison between the two lasers that have different focal spot sizes by normalizing the incident power over an area. The laser systems' output properties are compiled in Table S2 as an overview, linking laser power in mW, system percentage setting, and irradiance in kW cm^{-2}.

Figure 1e shows the absorption spectra of pristine and as-doped PBTTT thin films. The spectral positions of the 561 and 785 nm lasers are indicated by vertical lines. Doping with F_4TCNQ leads to a suppression of the neutral polymer absorption near 550 nm and gives rise to new absorption features near 420, 780, and 870 nm. The latter two peaks can be used for estimating the doping level. The peak at 420 nm is attributed to neutral F_4TCNQ, whereas the peaks near 770 and 870 nm are attributed to F_4TCNQ anions, overlapping with the broad P2 polaron band of PBTTT [28, 29, 34].

Laser induced de-doping is proposed to enable a reversal of the charge-transfer interactions of PBTTT and F_4TCNQ, generating neutral PBTTT and neutral F_4TCNQ species. Previous studies of F_4TCNQ-doped conjugated polymers have shown that long-range dopant transport and diffusion is dominated by neutral F_4TCNQ, whereas the ionized dopant remains comparatively immobile due

2365709x, 0, Downloaded from https://advanced.onlinelibrary.wiley.com/doi/10.1002/admt.71298, Wiley Online Library on [14/09/2026]. See the Terms and Conditions (https://onlinelibrary.wiley.com/terms-and-conditions) on Wiley Online Library for rules of use; OA articles are governed by the applicable Creative Commons License

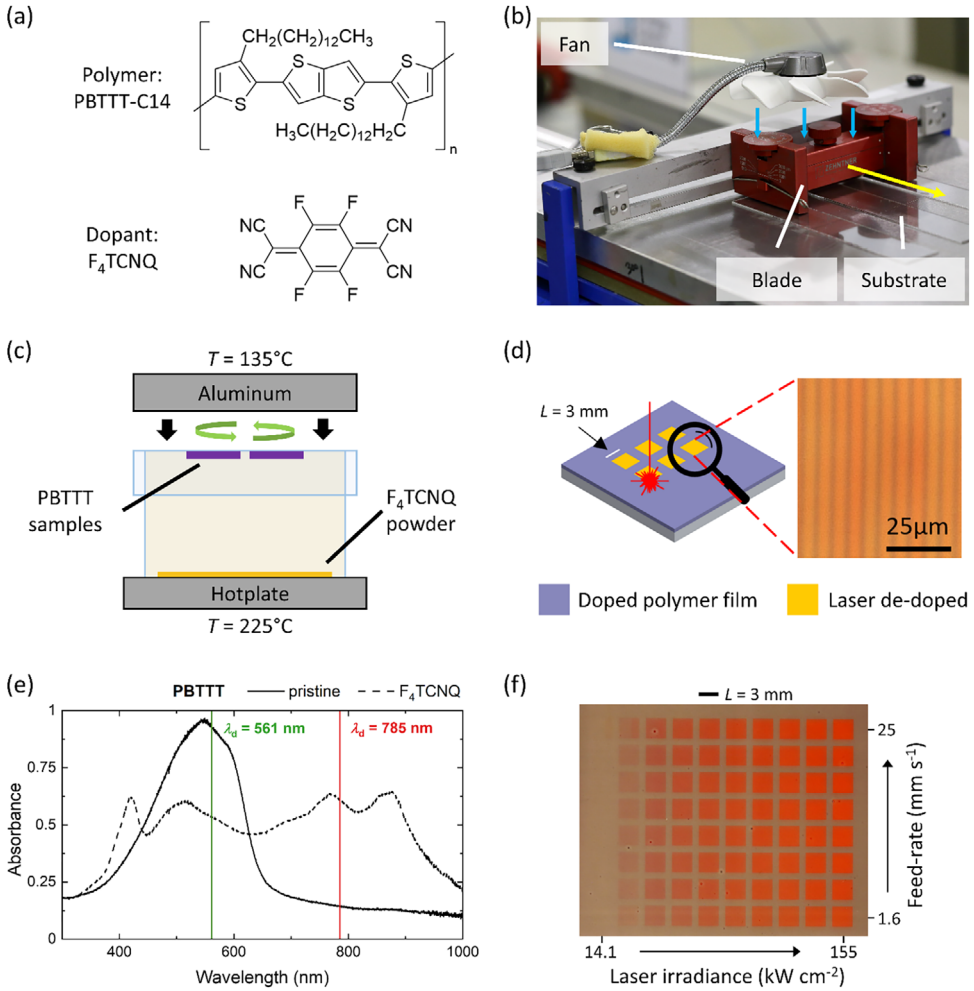

FIGURE 1 | (a) Chemical structures of the employed materials; polymer PBTTT and dopant F_4TCNQ. (b) Laboratory blade-coating setup with a temperature-controlled bed and a fan placed atop the blade, creating downward airflow during the coating process for accelerated drying. (c) Schematic of the PBTTT vapor-phase doping procedure with F_4TCNQ. The dopant is incorporated into the polymer by evaporation in a closed chamber formed by two glass containers. (d) Schematic of the de-doping approach using a focused laser beam to digitally pattern polymer thin films. (e) Absorption spectra of pristine (i.e. neutral, as-coated) PBTTT and the same films following doping with F_4TCNQ. Vertical lines indicate the spectral positions of the employed laser sources at $\lambda_d = 561$ and 785 nm that are used for de-doping. (f) Optical image of laser de-doped PBTTT film processed with different combinations of irradiance and feed-rate. De-doped areas can be identified by their orange color.

to strong Coulombic interactions with the polymer backbone [35, 36]. Consequently, thermally generated neutral F_4TCNQ can diffuse within the bulk of the film or sublimate from the irradiated area.

At 561 nm, laser radiation predominantly leads to photoexcitation of the neutral polymer followed by dissipation of heat to the adjacent dopant molecules. F_4TCNQ is relatively weakly bound in the polymer matrix [30, 37, 38] and, therefore, a sufficient temperature rise can lead to its local sublimation. As the absorption of the neutral polymer increases upon de-doping, the corresponding de-doping rate can be expected to progressively increase over the duration of laser exposure, since the suppressed polymer peak is restored toward the pristine case as de-doping happens.

In contrast, 785 nm irradiation is predominantly absorbed by the charged species, namely the PBTTT polarons and F_4TCNQ anions associated with the P2 absorption band, whereas the absorption of neutral PBTTT is negligible. Hence, we expect a gradual reduction of the de-doping rate over the exposure time due to decreasing absorption at 785 nm during de-doping.

The results of a combinatorial laser parameter screening using 785 nm laser excitation are shown in the image in Figure 1f. De-doping can be visually identified by a color change of the polymer film: while the as-doped film appears gray, de-doped film regions can appear orange (*amorphous* neutral PBTTT) or red/purple (*crystalline* neutral PBTTT). Both laser power and feed-rate are varied along the orthogonal axes of the 2D-array, with the laser-irradiated areas identified by an orange appearance. The laser feed-rate is varied from 1.7 to 25 mm s^{-1} along the vertical axis, and the laser's irradiance is varied from 14.1 to 155 kW cm^{-2} along the horizontal axis. Based on visual inspection, the impact of laser power is more significant than the feed-rate, as evidenced by the stronger color gradient along the horizontal axis of the 2D-array.

In a reference experiment presented in supplementary Figures S1 and S2, thermal de-doping of doped PBTTT films was performed

2365709x, 0, Downloaded from https://advanced.onlinelibrary.wiley.com/doi/10.1002/admt.71298, Wiley Online Library on [14/09/2026]. See the Terms and Conditions (https://onlinelibrary.wiley.com/terms-and-conditions) on Wiley Online Library for rules of use; OA articles are governed by the applicable Creative Commons License

on a hotplate under air and nitrogen atmospheres, followed by quenching to ambient temperature to approximate the rapid cooling of a laser-exposed film region with the underlying glass substrate acting as a heat-sink. As shown by the sample images and the corresponding UV–vis absorption spectra (Figures S1 and S2), thermal annealing at temperatures ≥ 300°C leads to a near-instantaneous de-doping (i.e., within the temporal resolution of the experiment). Annealing under ambient atmosphere additionally results in a progressive blueshift of the neutral polymer absorption band, indicating thermo-oxidative degradation of the polymer. In contrast, no comparable spectral shift is observed for annealing under nitrogen atmosphere, demonstrating significantly improved resistance to degradation in the absence of oxygen. Therefore, these references provide a spectroscopic benchmark for the characteristics of PBTTT:F_4TCNQ films de-doped by laser irradiation. Importantly, all laser de-doping experiments discussed during this work are performed in air only, since, in its default configuration, the machine cannot be flooded with nitrogen to provide an inert atmosphere.

2.2 | UV–Vis Analysis of Polymer Films

To deepen our understanding of how laser processing influences the doping level in the polymer films, we systematically examined a series of processing conditions using UV–vis spectroscopy. When the focused laser irradiates the material and photoexcitation occurs, typical spectral changes can be identified, as visualized using the UV–vis spectra shown in Figure 2a, for pristine and as-doped references as well as the laser de-doped material. First, a blueshift of the main absorption peak of PBTTT from 560 to 500 nm is observed. Interestingly, this blueshift is invariant with laser irradiance, which, by reference to the absorption spectra shown in Figure S2, obtained for films annealed under inert and ambient atmospheres, indicates that the primary contributing factor is likely to be a change of the polymer to a more amorphous microstructure. This is further corroborated by the disappearance of the absorption shoulder at approximately 600 nm for films that have undergone laser processing. While some degree of polymer degradation arising from intra-chain oxidation and chain scission is also likely to occur [39, 40], this process would be expected to result in a more progressive absorption blueshift with increasing irradiance or decreasing feed-rate. These observations point to the scenario that PBTTT is locally heated by photothermal conversion to a temperature above its ∼230°C melting point. As the laser then moves along the sample, the extremely fast cooling resulting from the presence of the substrate effectively vitrifies the polymer in a pre-dominantly amorphous state [41] below its ∼100°C glass transition temperature. We do not exclude the possibility that some degree of molecular ordering could be recovered through a subsequent post-processing step, such as a controlled thermal process or a rapid exposure to moderately swelling solvents. Second, the pronounced decrease of the absorption features near 770 and 870 nm, accompanied by the recovery of the peak near 500 nm, signifies de-doping and reduction of F_4TCNQ anion density in the bulk of the film [29].

As introduced previously in Figure 1f, the de-doping process in the parameter-screening experiment was controlled by two variables: laser irradiance and feed-rate. UV–vis spectra were recorded in the center of each de-doped region. Representative spectra are plotted in Figure 2a. In Figure 2a panel (i), the laser irradiance was varied from 14.1 to 155 kW cm^{-2} at a constant feed-rate of $\nu = 1.7$ mm s^{-1}. Panel (ii) shows the corresponding measurements at a faster feed-rate of 25 mm s^{-1} over the same irradiance range.

To quantitatively describe the extent of de-doping, we defined a de-doping ratio R_d, and extracted it from the data acquired from the two-dimensional parameter map shown in Figure 1f. This metric captures the relative suppression of the 767 nm peak compared to pristine and as-doped references and is defined as:

$$R_d\ (767\ \text{nm}) = \frac{A_{\text{as–doped}} - A_{\text{de–doped}}}{A_{\text{as–doped}} - A_{\text{pristine}}} \tag{3}$$

Here, A_{pristine} and $A_{\text{as – doped}}$ denote the peak absorbance of the pristine and as-doped films at 767 nm, respectively, while $A_{\text{de – doped}}$ denotes the absorbance after laser exposure. A higher R_d value corresponds to a greater degree of de-doping. The spatially resolved analysis is visualized in Figure 2b. The R_d values for a laser power sweep at both feed-rates from (a) are plotted in Figure 2c. From the recorded UV–vis data, it is evident that the laser irradiance plays a substantially more significant role than the feed-rate. For a fixed irradiance, spectra recorded at $\nu = 1.7$ and 25 mm s^{-1} are very similar, whereas at constant feed-rate the spectra change significantly as the irradiance increases from 14.1 to 155 kW cm^{-2}. This trend is illustrated clearly in Figure 2c, where the curves for the two feed-rates nearly overlap. In addition to the data shown in Figure 2, the evolution of R_d for a feed-rate sweep at fixed laser irradiance, as well as the full array with all extracted R_d values, are shown in Figure S4.

We conclude that the de-doping process is pre-dominantly governed by laser irradiance (i.e. temperature rise) rather than dwell time (i.e. kinetics). For all subsequent experiments, we employed the maximum system-supported feed rate of $\nu = 30$ mm s^{-1}.

To determine the minimum irradiance required to initiate de-doping, we performed a systematic irradiance sweep using the 785 nm laser. UV–vis spectra were recorded in 15 equidistant steps from 0 to 22.3 kW cm^{-2} (0%–15% of the maximum system-supported power), as shown in Figure 2d. At low irradiance, the spectra remain unchanged relative to the as-doped reference. Upon exceeding a critical irradiance, the characteristic signatures of de-doping emerge, namely attenuation of the absorption peaks near 420, 770, and 870 nm, as well as recovery and blueshift of the polymer peak near 560 nm. Tracking the evolution of the peaks at ∼770 and ∼870 nm yields the double-logarithmic plot shown in Figure 2e. A linear regression fit reveals a clear threshold behavior, corresponding to an onset de-doping threshold of approximately 12.3 kW cm^{-2}, as summarized in Table 1:

Below this threshold, no spectral changes indicative of de-doping can be detected. Above it, the doping level decreases progressively with increasing irradiance, as reflected in the gradually diminishing intensities of the absorption features near 770 and 870 nm.

2365709x, 0, Downloaded from https://advanced.onlinelibrary.wiley.com/doi/10.1002/admt.71298, Wiley Online Library on [14/09/2026]. See the Terms and Conditions (https://onlinelibrary.wiley.com/terms-and-conditions) on Wiley Online Library for rules of use; OA articles are governed by the applicable Creative Commons License

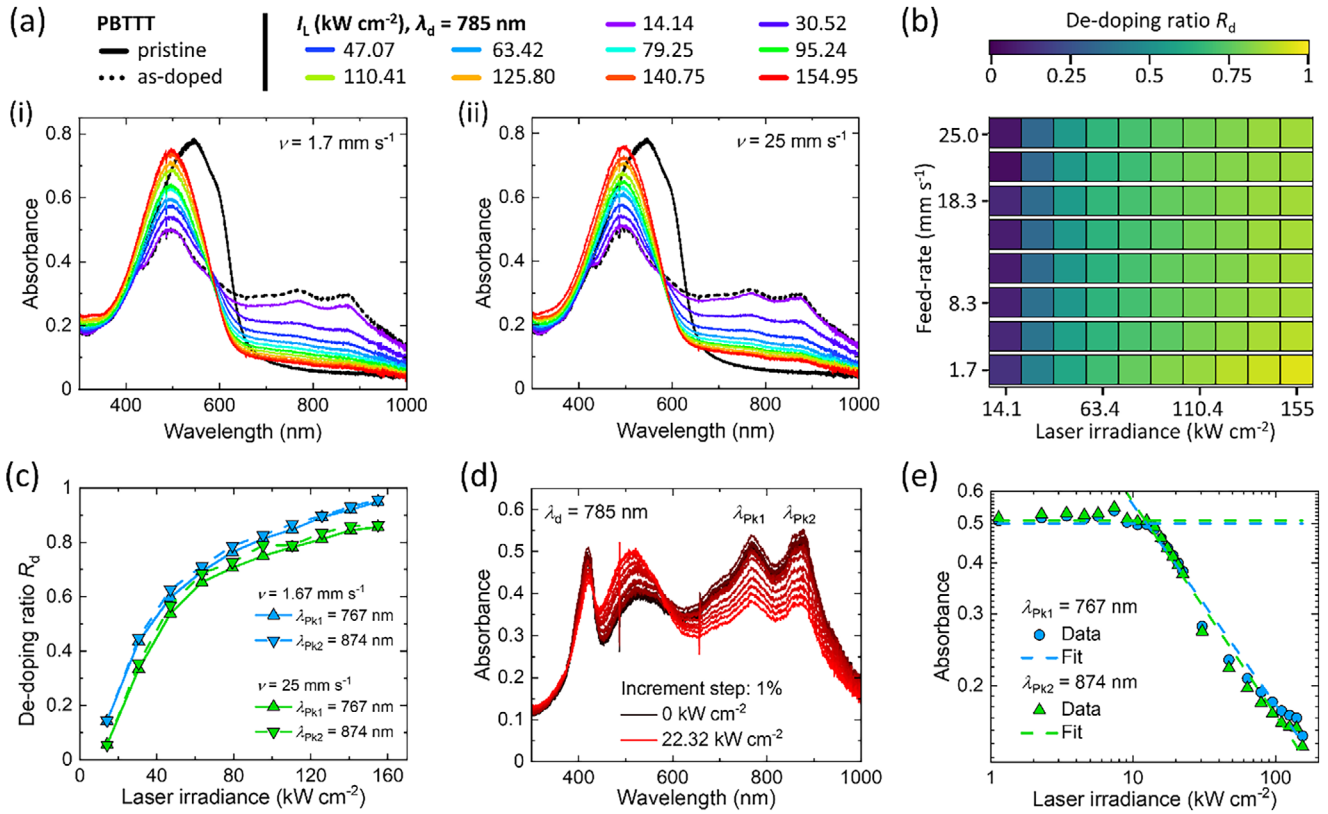

FIGURE 2 | (a) UV–vis spectra acquired from the sample shown in Figure 1f for de-doping performed at constant feed rate and increasing laser irradiance. Panel (i) shows data for $\nu = 1.7$ mm s^{-1}, while panel (ii) shows data for $\nu = 25$ mm s^{-1}. (b) Scatter-plot visualization of the degree of de-doping achieved by laser processing. The absorption peak near 770 nm is compared against pristine and as-doped reference spectra, and the resulting calculated de-doping ratio R_d is represented by color coding. (c) Degree of de-doping as a function of laser irradiance for $\nu = 1.7$ and 25 mm s^{-1}, extracted from the peaks λ_{Pk1} and λ_{Pk2} near 770 and 870 nm in the spectra shown in panel (a). (d) UV–vis spectra of PBTTT films de-doped using low laser irradiances at λ_d = 785 nm. The two above-mentioned spectral peaks are labelled. (e) Double-logarithmic analysis of the peak absorbance values near 770 and 870 nm as a function of laser irradiance. A linear regression fit enables extraction of the de-doping onset threshold.

TABLE 1 | Extracted de-doping thresholds for λ_d = 785 nm.

Spectral peak [nm]	De-doping threshold [kW cm^{-2}]
767	12.39
874	12.18

2.3 | Influence of Laser Wavelength

Next, samples were prepared to investigate the effect of using 561 nm radiation for de-doping, and to characterize the electrical properties of the processed films.

As previously discussed and visualized in Figure 1e, the choice of laser wavelength is expected to influence the de-doping process and the resulting material characteristics. To investigate this, samples on glass substrates were prepared by blade-coating, and doped following the procedure described in the Experimental section. The two different excitation wavelengths, 785 and 561 nm were used to de-dope the films using a series of increasing laser power settings in the range of 14–155 and 27–254 kW cm^{-2}, respectively. In Figure 3a the corresponding photograph of the sample is shown. The areas de-doped by laser radiation are 3 × 3 mm^{-2} in size and can be identified by their color. Direct comparison of two areas de-doped with comparable laser irradiance of approximately 155 kW cm^{-2}, but different laser wavelengths, reveals a stronger de-doping effect for 561 nm radiation, as indicated by the more intense orange coloration. For high laser irradiance, the green laser induces strong heating and irreversible degradation of the polymer [42]. The thin film turns transparent, as seen in the lower right-hand corner of the optical image in Figure 3a. For all of the laser-treated areas shown in panel (a), UV–vis spectra are recorded at the center of each patterned region, with the corresponding data shown in Figure 3b. The top panel shows the results for λ_d = 785 nm, the bottom panel for λ_d = 561 nm. The measurement data for the 785 nm laser follows the trends already observed and established in Figure 2a: With increasing laser irradiance, the PBTTT film is increasingly de-doped and recovering its pristine state, albeit with the above-noted absorption blueshift. For the 561 nm laser, the behavior is comparable, but stronger de-doping can be observed when compared to NIR excitation. As quantifiable proof, the de-doping ratio is extracted based on the UV–vis data and results in R_d = 0.8 and 0.88 for λ_d = 785 and 561 nm respectively at I_L = 155 kW cm^{-2}.

The areas de-doped with very high 561 nm irradiance reveal a drastic shift in the films' spectra, as can be seen in the lower panel of Figure 3b. In this case we observed – in line with the

2365709x, 0, Downloaded from https://advanced.onlinelibrary.wiley.com/doi/10.1002/admt.71298, Wiley Online Library on [14/09/2026]. See the Terms and Conditions (https://onlinelibrary.wiley.com/terms-and-conditions) on Wiley Online Library for rules of use; OA articles are governed by the applicable Creative Commons License

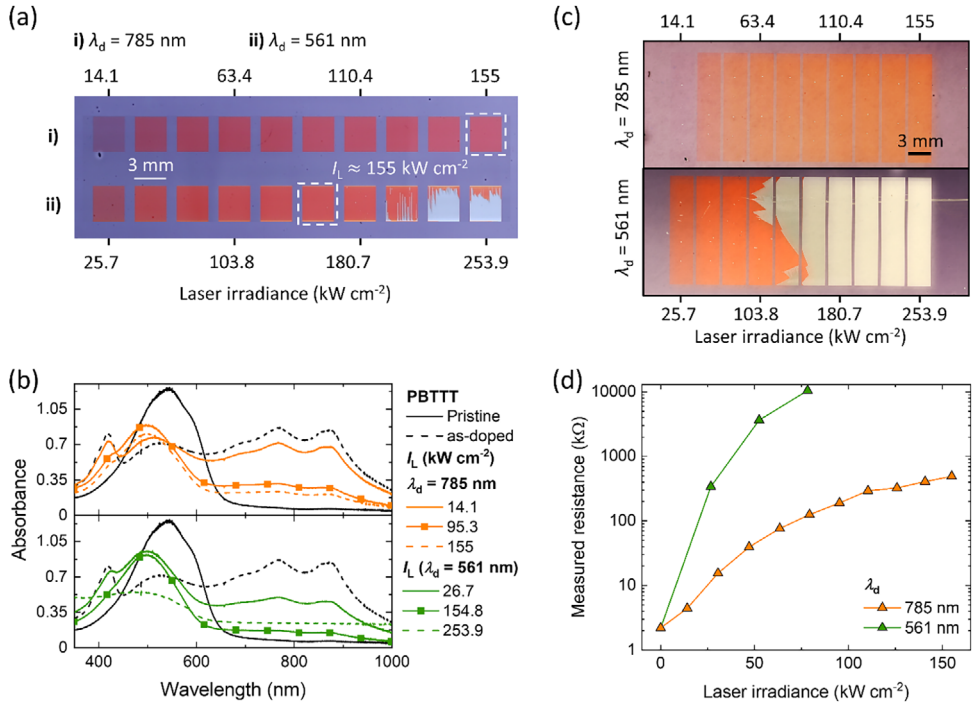

FIGURE 3 | (a) Optical image of a PBTTT thin film doped with F_4TCNQ, showing regions that have been locally de-doped using focused laser irradiation. The upper and lower rows correspond to de-doping performed with λ_d = 785 and 561 nm excitation, respectively. Two representative regions treated at similar irradiance levels are highlighted. (b) UV–vis absorption spectra acquired from the sample shown in panel (a). The curves display the spectral evolution of PBTTT upon de-doping with increasing laser irradiance at $\lambda_d = 561$ nm (bottom panel) and $\lambda_d = 785$ nm (top panel). (c) Photograph of the sample used for electrical resistance measurements. The top row was de-doped using 561 nm excitation, and the bottom row using 785 nm excitation, with laser irradiance increasing from left to right. De-doping at 561 nm using high irradiances above 130 kW cm^{-2} induces an irreversible modification of the polymer, evidenced by a distinct color change of the film. (d) Electrical resistance of the polymer thin films shown in panel (c), plotted on a semi-logarithmic scale for both de-doping wavelengths.

already mentioned transition to a transparent state – increased absorption below 400 nm. A reference experiment using thermal de-doping on a hotplate was carried out, results of which are shown in supplementary Figures S1 and S2. UV–vis spectra of samples de-doped at varying temperatures ranging from 200°C to 350°C in both air and nitrogen atmosphere are shown for different treatment times. Comparing the hotplate reference experiment and data with the laser-based approach, we observed that the behavior is very similar, both in terms of color impression as well as the spectral evolution of the recorded UV–vis spectra. We also note, that the blueshift of the main PBTTT peak is progressive for annealing in air atmosphere, indicating that the laser process can indeed trigger thermo-oxidative processes, especially when using very high-intensity radiation at 561 nm. Overall, the laser-based de-doping process induces degradation regardless of the laser parameters.

One experiment aimed at attempting to restore some of the lost crystallinity and molecular order due to the laser processing has been performed, the results of which are summarized in Figure S3. From the gathered UV–vis it can be seen that a post-thermal treatment can induce a redshift of the polymer absorption peak back toward 560 nm. However, the process also leads to a significant amount of additional de-doping, visible in the suppression of the 780 and 870 nm spectral features, as well as a color change in the optical image. As such, the process needs additional refinement to reach a viable outcome. Moreover, residual ionized F_4TCNQ absorption features can still be observed even at high laser irradiation since the spectral absorption near 780 and 870 nm does not fully approach the pristine spectrum. In contrast, our hotplate de-doping reference experiment from Figure S2 shows that a more complete degree of de-doping can be achieved, where the absorption near 780 and 870 nm closely approaches the pristine case, resulting in R_d values close to 1. We suspect that the swath-based de-doping approach is not fully homogeneous, which will be examined in further detail below using spectroscopic Raman mapping as well as SEM analysis.

2.4 | Electrical Characterization

In order to characterize the electrical properties of laser-treated polymer films, their electrical resistances were measured using a 4-point probe setup. An optical image of the measured sample is shown in Figure 3c. In the top part of the image, the film de-doped with 785 nm laser is shown, whereas in the bottom part the polymer de-doped with a 561 nm is shown; in both cases the laser irradiance increases from left to right. The corresponding measured electrical resistance values are shown in Figure 3d. Initially, the as-doped film has a resistance value of 2.2 kΩ. When de-doped with the 785 nm laser, the resistance increased consistently with laser irradiance, from 4.4 to 490 kΩ. De-doping with the 561 nm laser caused the resistance to rise from 340 kΩ to 10.5 MΩ for the irradiance range of 27.2–78.2 kW cm^{-2}. For higher

2365709x, 0, Downloaded from https://advanced.onlinelibrary.wiley.com/doi/10.1002/admt.71298, Wiley Online Library on [14/09/2026]. See the Terms and Conditions (https://onlinelibrary.wiley.com/terms-and-conditions) on Wiley Online Library for rules of use; OA articles are governed by the applicable Creative Commons License

irradiance, the PBTTT film changes irreversibly, losing virtually all absorption in the visible range, as can be seen in the optical image in Figure 3c.

Overall, the 785 nm laser allowed a change in electrical resistance over 2 orders of magnitude, while the 561 nm laser enabled tuning over almost 5 orders of magnitude. The resistance value of the pristine PBTTT film could not be measured with our setup, indicating that the value is larger than 200 MΩ. While transistor-based characterization could potentially provide additional insights into the corresponding free-carrier density, the substantial microstructural and morphological changes accompanying laser-induced de-doping would require careful separation of doping, mobility, and contact-resistance effects. Accordingly, a rigorous device-level investigation is being pursued as a continuation of the present work and lies beyond the scope of this manuscript.

2.5 | Spectroscopic Raman Analysis

The local laser-induced evolution of microstructure and doping level are next studied with spectroscopic Raman mapping. This technique has been extensively used for quantitative analysis of macroscopic and local doping in organic semiconductor films owing to its diffraction-limited spatial resolution and chemical-species-selective excitation and detection.

Below we focus on a PBTTT film de-doped using λ_d = 785 nm and constant feed-rate ν = 30 mm s^{-1}. Raman analysis is performed using excitation at 488 nm which enables resonance enhancement by coinciding with the absorption of neutral, pre-dominantly amorphous PBTTT (see absorption spectra in Figure 1e) and has been previously used for quantitative analysis of doping levels in PBTTT doped with F_4TCNQ [15] and other dopants [27]. The Raman features relevant to the following discussion are labeled 'R1' through 'R3'. Peak R1 at 1393 cm^{-1} is assigned to a C═C stretching mode of the thienothiophene core, peak R2 at 1494 cm^{-1} corresponds to the PBTTT backbone C═C/C─C stretching mode whose relative intensity is sensitive to the polymer doping state and has previously been associated with polaron formation on the PBTTT backbone [43], and peak R3 at 1642 cm^{-1} originates from neutral or ionized F_4TCNQ [21].

The de-doped array is shown in Figure 4a, with irradiance I_L increasing from 14.1 to 155.0 kW cm^{-2} along the horizontal axis and interline laser swath spacing d varying from 1 to 10 µm along the vertical axis (as indicated). An image of an exemplary de-doped area (I_L = 30.5 kW cm^{-2}, d = 10 µm) is shown in Figure 4b, highlighting the positional accuracy of successive laser swaths and the absence of large F_4TCNQ surface crystals that are known to form during thermal de-doping [30].

For the same de-doped area, Figure 4c shows a map of the ratio of maximum intensities of the peaks R1 and R3 at 1393 and 1642 cm^{-1} respectively. While previous reports employed the intensity ratio of R1 and R2 Raman peaks to quantify conductivity within PBTTT films [15, 27], we instead focus of the R3/R1 ratio because it is likely to be less sensitive to any microstructural changes of PBTTT, given that the R3 peak directly probes the presence of any residual F_4TCNQ in the polymer matrix. The corresponding Raman intensity map shows a clear modulation of R3/R1 Raman intensity ratio, reaching its minimum values at the centers of laser-irradiated regions. As an additional confirmation of de-doping, a map of total integrated PL intensity recorded with excitation at 532 nm (coinciding with absorption of neutral PBTTT) is shown in Figure 4d. Indeed, a strong PL enhancement can be observed at the de-doped, laser-exposed regions, while the PL intensity is quenched in the areas between laser swaths.

Figure 4e compiles average Raman spectra recorded for the centers of laser de-doped regions as a function of laser irradiance I_L of the de-doping laser with λ_d = 785 nm and compares them with reference spectra measured for pristine and as-doped PBTTT. The Raman spectra of de-doped PBTTT reach a close overlap with the reference pristine PBTTT spectrum already for a de-doping intensity of I_L = 30.5 kW cm^{-2}, with a minor relative attenuation of the 1393 cm^{-1} mode. We investigated this attenuation in a control experiment, where F_4TCNQ-doped PBTTT films were annealed at temperatures ≥ 350°C under ambient and inert atmospheres (Figure S5). The results suggest that the primary contributing factor to the relative attenuation of the 1393 cm^{-1} is the change of laser-irradiated PBTTT to a more amorphous microstructure, with an additional minor contribution from thermo-oxidative degradation – consistent with the results of absorption spectroscopy presented in supplementary Figures S1 and S2. Examining the C-H_2 stretching mode of the PBTTT alkyl side chains in the high-frequency 2400–3200 cm^{-1} region (Figure S6) reveals a minor decrease in the relative intensity of backbone vibrational modes in comparison to the 2900 cm^{-1} feature. This observation further corroborates that some degradation of the conjugated polymer backbone accompanies the laser de-doping process.

A plot of the R3/R1 Raman intensity ratio for the laser-exposed regions as a function of I_L is shown in Figure 4f. The relative contribution from F_4TCNQ anions reaches a minimum at I_L = 30.5 kW cm^{-2} and remains constant upon further increase of optical power, with a clear signature of F_4TCNQ presence even at maximum de-doping irradiance (with respect to the pristine reference sample).

In Figure 4g, the photothermal de-doping process is further examined by spatial profiling of the R3/R1 Raman intensity ratio across laser swaths with an interline spacing of d = 10 µm as a function of I_L. The data shows an abrupt change of the R3/R1 profile shape between I_L = 14.1 and I_L = 30.5 kW cm^{-2} which is indicative of pronounced lateral heat propagation within the film during the de-doping process. Interestingly, the maximum R3/R1 ratio exceeds that of the reference as-doped films in the regions between the laser swaths for I_L = 14.1–63.4 kW cm^{-2}, which indicates migration of F_4TCNQ away from the laser-exposed regions into the non-exposed regions by, e.g., evaporation and re-deposition. In addition, mapping analysis of the Raman R1/R2 Raman intensity ratio confirmed that a spatially homogenous degree of de-doping can be achieved by a combination of laser power and interline spacing, as illustrated in Figure S7.

In summary, the insights gained from spectroscopic Raman mapping indicate that the laser-based de-doping process is efficient yet incomplete, with F_4TCNQ concentration in the film reaching its minimum value at relatively low laser irradiances

2365709x, 0, Downloaded from https://advanced.onlinelibrary.wiley.com/doi/10.1002/admt.71298, Wiley Online Library on [14/09/2026]. See the Terms and Conditions (https://onlinelibrary.wiley.com/terms-and-conditions) on Wiley Online Library for rules of use; OA articles are governed by the applicable Creative Commons License

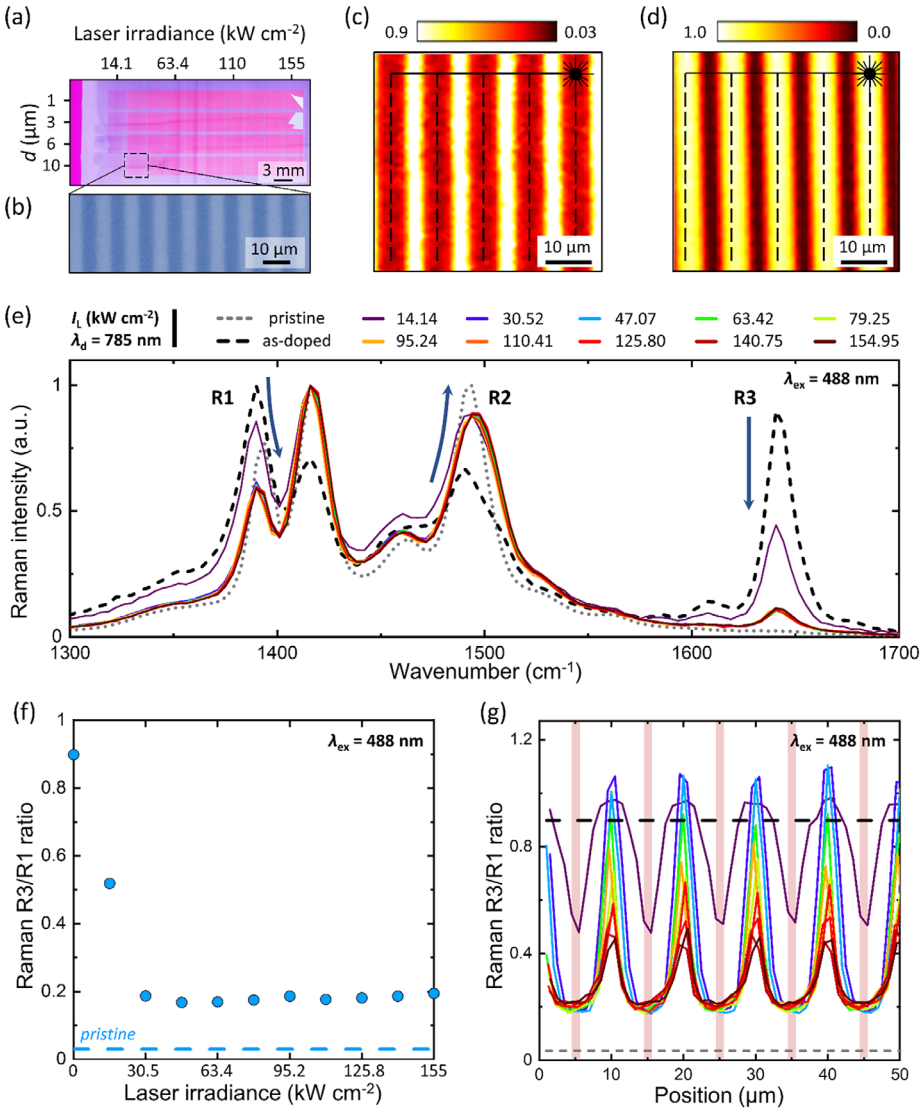

FIGURE 4 | (a) Image of a PBTTT film containing an array of areas de-doped using $\lambda_d = 785$ nm laser excitation and constant feed-rate $v = 30$ mm s^{-1} with varying incident irradiance I_L and interline laser swath spacing d. (b) Micrograph of an area de-doped using $I_L = 30.5$ kW cm^{-2} and d = 10 μm. Also shown for the same laser parameters are: (c) Raman map of R3/R1 peak intensity ratio recorded with excitation at 488 nm and (d) map of total integrated PL intensity (550–800 nm) recorded with excitation at 532 nm. In both panels, dashed lines indicate the centers of individual laser swaths. (e) Raman spectra recorded at the center of laser-exposed areas as a function of I_L, as well as reference spectra for pristine and as-doped PBTTT, for 488 nm Raman excitation. Selected Raman peaks (R1, R2, and R3) used in the analysis are highlighted; arrows are a guide to the eye for spectral changes occurring with increasing I_L. (f) R3/R1 Raman intensity ratio as a function of I_L corresponding to the spectra in (d). The dashed line indicates the reference value for the pristine, non-doped sample. (g) Profiles of the R3/R1 Raman intensity ratio as a function of de-doping laser irradiance I_L at $\lambda_d = 785$ nm (interline spacing of laser swaths d = 10 μm). Vertical red markers indicate the positions of the laser swaths; horizontal dashed and dotted markers indicate the R3/R1 values for as-doped and pristine reference films, respectively.

and remaining invariant upon further irradiance increase. While the origins of this are unclear, it is likely that the adopted doping thermally-assisted vapor-phase doping process leads to a moderate fraction of charge transfer complex (CTC) doping. Previous reports further demonstrated [30] that CTC dopants exhibit a substantially higher thermal stability than integer charge transfer (ICT) dopants. An additional factor contributing to a minor residual doping level within laser-irradiated regions, including those with a close overlap of adjacent laser swaths, is likely to be the re-deposition of the sublimated F_4TCNQ molecules onto the sample during the process, followed by automatic re-doping of PBTTT. Introducing laminar airflow over the sample during laser irradiation could be a pathway to reduce this re-doping process. For completeness, the corresponding Raman analysis of a PBTTT sample de-doped using $\lambda_d = 561$ nm irradiation is presented in Figure S8, showing similar observations to those discussed above.

2.6 | SEM Analysis

To investigate laser-induced de-doping within the focal region of single written lines, we employed scanning electron microscopy (SEM). SEM enables (sub)-micrometer-scale visualization of contrast arising from local variations in electrical

2365709x, 0, Downloaded from https://advanced.onlinelibrary.wiley.com/doi/10.1002/admt.71298, Wiley Online Library on [14/09/2026]. See the Terms and Conditions (https://onlinelibrary.wiley.com/terms-and-conditions) on Wiley Online Library for rules of use; OA articles are governed by the applicable Creative Commons License

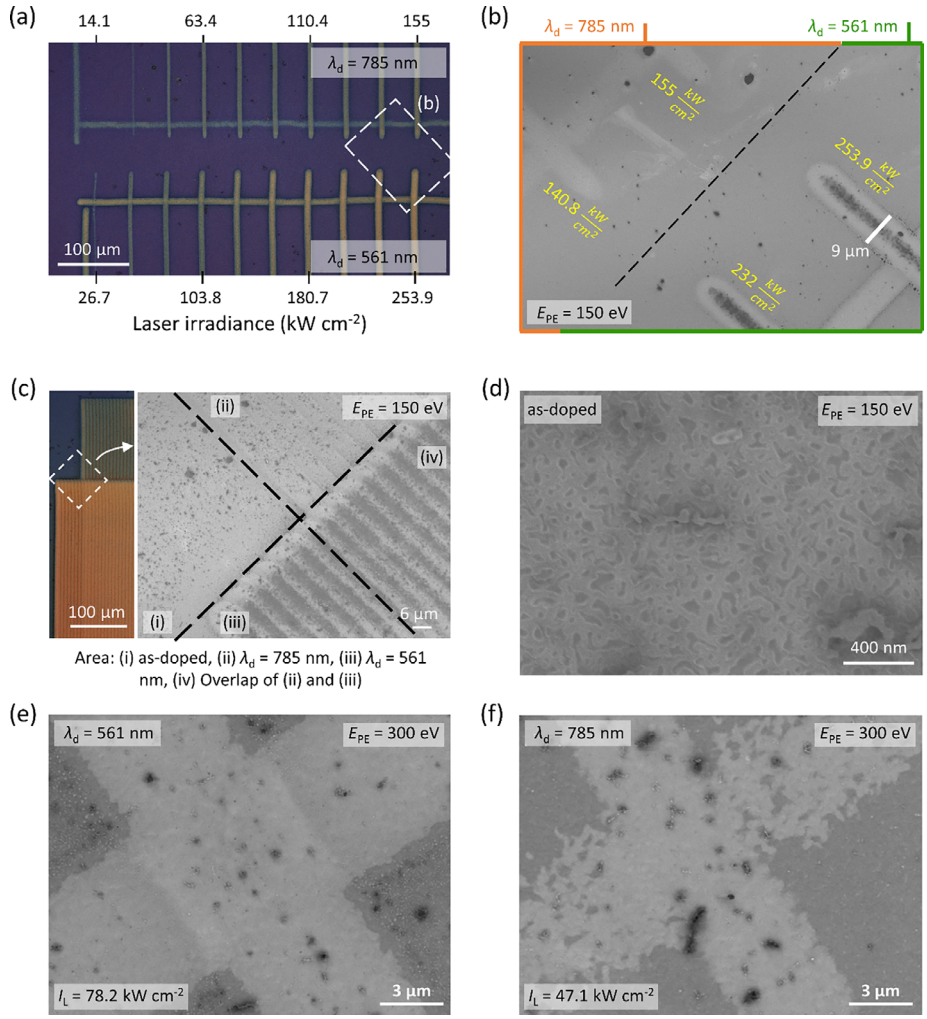

FIGURE 5 | (a) Optical image of digitally de-doped lines written into a PBTTT thin film using a focused laser beam at de-doping wavelengths λ_d = 561 and 785 nm for I_L = 26.7–254.0 and 14.1–155.0 kW cm^{-2}, respectively. (b) SEM image of the laser-irradiated region highlighted in panel (a), showing the de-doped line patterns produced utilizing both wavelengths. (c) Left: Optical image of PBTTT de-doped via a raster-scan area patterning using both de-doping wavelengths λ_d. Right: Corresponding SEM image of the region indicated by the white box, displaying the juxtaposition of the as-doped and laser de-doped areas. (d) High-resolution SEM image of PBTTT doped with F_4TCNQ in the absence of laser exposure (as-doped reference). (e) SEM image of locally de-doped, intersecting laser-written lines generated using 561 nm excitation and (f) 785 nm excitation.

conductivity/charging, which in turn reflect the differences in doping level. Images were acquired using a low-energy electron beam (150–300 eV), and representative results are shown in Figure 5. For this study, both the 561 and 785 nm lasers were used within the irradiance ranges established earlier and summarized in Table S2. PBTTT films were prepared on undoped, double-side-polished silicon substrates, to enable imaging without needing to cover the samples with a conductive layer.

Figure 5a shows an optical image of a sample displaying single laser-written de-doped lines with irradiance increasing from left to right, and the corresponding SEM image of the highlighted region in Figure 5b. The image reveals defined doping modulation with a lateral feature size of approximately 9 µm, which is less than the theoretical feature size estimated in Table S1. For the shown lines, de-doping with λ_d = 785 nm was performed with I_L = 141 and 155 kW cm^{-2}, while de-doping with λ_d = 561 nm used 232 and 254 kW cm^{-2}, as indicated by the labels in Figure 5b. At the center of the laser 561 nm written line, dark spots can be seen, originating from electron-beam-induced charge accumulation, which indicates reduced local electrical conductivity due to decreased dopant concentration. We attribute this sub-resolution gradient within the patterned line to a local effect caused by the gaussian nature of the beam and the intense irradiation.

To examine larger-area modifications, we generated de-doped regions of 0.2 × 1 mm^2 using raster-scan patterning in the established laser irradiance ranges. The resulting optical and SEM images of one exemplary area are shown in Figure 5c. The SEM image (right) corresponds to the white-boxed area in the optical image. Area (i) shows the as-doped material, while area (ii) was de-doped using 785 nm with I_L = 125.8 kW cm^{-2} and (iii) with 561 nm at I_L = 206.3 kW cm^{-2}. Area (iv) is an overlap of (ii) and (iii). Darker regions in the image – associated with charge accumulation – indicate lower electrical conductivity. Even though we previously observed a mostly homogenous dopant profile with the correct interline spacing and irradiation

2365709x, 0, Downloaded from https://advanced.onlinelibrary.wiley.com/doi/10.1002/admt.71298, Wiley Online Library on [14/09/2026]. See the Terms and Conditions (https://onlinelibrary.wiley.com/terms-and-conditions) on Wiley Online Library for rules of use; OA articles are governed by the applicable Creative Commons License

combination in our Raman analysis from Figure 4 and Figure S7, the alternating dark and bright lines, particularly visible in the area exposed to λ_d = 561 nm, seem to indicate that the process is not fully homogenous. Even with overlapping laser swaths, each line can still be identified individually, even in the optical microscope image. One possible explanation could be the previously mentioned re-deposition of sublimated F_4TCNQ close to the laser line and subsequent re-doping of PBTTT. Another explanation could be found in the silicon substrate of the SEM samples, which alters the thermal behavior of the process compared to glass.

Figure 5d presents a high-magnification SEM image of the as-doped polymer film. A connected network structure with characteristic dimensions of ~50 nm can be observed, reflecting the morphology of the ordered polymer, similar to what other reports have observed using atomic force microscopy (see Supporting Information of [34] and [32]). In the image, areas with a brighter color represent higher conductivity, suggesting the presence of dopant molecules within the polymer matrix.

Figure 5e shows a high-resolution SEM image of crossing lines created using the 561 nm laser at 78 kW cm^{-2}. It exhibits a largely homogenous central region with an approximately 1 µm wide transition zone along its edges. Figure 5f is a similar SEM image, this time showing two crossing lines that have been created using the 785 nm laser at 47 kW cm^{-2}. In contrast to panel (e), the line appears less homogenous and lacks a distinct boundary. We attribute this difference to the stronger absorption of 561 nm laser radiation by the polymer backbone, whereas the 785 nm radiation is primarily absorbed by the ionized dopant species rather than the polymer itself. The mesoscale pattern visible here resembles the network-like structure observed in Figure 5c, albeit at a larger scale.

Taken together, the SEM results demonstrate that local modulation of doping strength and electrical conductivity with micrometer-scale resolution is achievable using laser irradiation. The analysis also supports the claim of the distinct interactions of the two de-doping wavelengths with the polymer-dopant system: the 561 nm laser is strongly absorbed by the polymer matrix and backbone, while the 785 nm laser pre-dominantly excites the dopant anions. These differences manifest in the spatial uniformity and morphology of the de-doped regions.

3 | Conclusion and Outlook

We have successfully demonstrated the control of doping concentration and electrical conductivity with a laser-defined resolution down to 9 µm and below in a fully digital process conducted in ambient air. SEM analysis, Raman and PL intensity mapping of laser-treated PBTTT films confirm micrometer-scale patterning of conductivity. Consistent, observable and repeatable trends for de-doping were recorded and analyzed using UV–vis and Raman spectroscopy measurements.

Based on the collected optical, electrical, and spectroscopic data, we propose that laser-induced de-doping proceeds via photothermal heating of the polymer-dopant system, resulting in a partial reversal of the charge-transfer interaction between PBTTT and F_4TCNQ. The resulting neutral F_4TCNQ species are expected to exhibit substantially greater mobility than their ionized counterparts and can therefore diffuse within the film, re-dope adjacent cooler regions, or sublimate from the irradiated area. Evidence supporting this interpretation includes the observed redistribution of dopant species in Raman maps, the incomplete but reproducible removal of F_4TCNQ signatures from UV–vis and Raman spectra, and the agreement with thermally induced de-doping behavior observed in the control experiments conducted on a hotplate. While some degree of dopant decomposition under extreme processing conditions cannot be completely excluded, the available results indicate that thermally activated dopant transport and removal constitute the dominant de-doping pathway.

Among the possible control parameters and processing conditions, the choice of laser wavelength significantly impacts the process. A green cw-laser at 561 nm results in stronger de-doping of the polymer thin films and allows for a larger range of electrical resistance control, spanning 5 orders of magnitude. However, this choice of laser irradiation also leads to stronger degradation and a higher loss of crystallinity. In contrast, using our NIR laser at 785 nm enables changes in electrical resistance by two orders of magnitude, with less severe degradation of the polymer thin films. The range might be extended further using a higher power laser system.

A full reversal of the doping process, however, could not be achieved in the scope of this work, even at very high laser irradiances. This limitation is attributed to the inhomogeneities in the laser process when treating larger areas (such as re-doping of adjacent areas) and the unavoidable degradation effects as a result of high-intensity laser irradiation and thermo-oxidative effects.

Experiments to further investigate aspects of the presented approach could include mild post-irradiation solvent treatment via blade-coating of i.e., acetonitrile, in order to remove any residual dopant in laser-treated areas. Furthermore, post-processing strategies such as moderate thermal annealing or solvent-vapor annealing may provide a pathway to partially recover polymer ordering after laser-induced de-doping. While this possibility was only briefly investigated in the present work, refinement of experimental conditions may lead to recovery of the redshifted absorption features without further de-doping. This restoration of increased molecular order would be an interesting topic for future study. Effects such as chain scission and oxidation may not be recoverable, so it may offer interesting insights into the interplay and ratios of these effects.

The laser process could be further optimized by being carried out under a local nitrogen-rich atmosphere via blanket gas flow – which could also reduce re-deposition of sublimated F_4TCNQ adjacent to the laser's path. Furthermore, material systems with lower thermal stability of doping, such as P3HT or PBTTT doped with $FeCl_3$ [28] could be investigated. Exploration of amorphous polymers such as C16-IDTBT doped with the Lewis acid BCF [44] could also be interesting and reveal new application cases and process properties. Another interesting investigation could be exploring the transfer of the presented method to a material system with stable bulk doping based on F6-TCNNQ.

2365709x, 0, Downloaded from https://advanced.onlinelibrary.wiley.com/doi/10.1002/admt.71298, Wiley Online Library on [14/09/2026]. See the Terms and Conditions (https://onlinelibrary.wiley.com/terms-and-conditions) on Wiley Online Library for rules of use; OA articles are governed by the applicable Creative Commons License

One advantage of the presented laser-based de-doping approach lies in its compatibility with industrial-scale processing and, consequently, its potential for upscaling of functional devices such as i.e. OFETs. In particular, the method opens a promising route for managing contact resistance of such devices: dopants could first be deposited by inkjet printing in the vicinity of the source and drain contacts, followed by laser-assisted de-doping to locally sharpen and refine the doping profiles according to requirements. This two-step strategy would enable sub-printing resolution control of the dopant while retaining the throughput advantages of scalable printing techniques. A particularly interesting subject for future work would be the correlation of laser processing conditions with transistor characteristics such as threshold voltage, contact resistance, carrier mobility, and effective charge-carrier density in fully functional OFET devices.

4 | Experimental Section

4.1 | Materials

Solutions for blade-coating were prepared inside a nitrogen-filled glovebox. PBTTT-C14 (1-material, CAS: 888491-19-8) was dissolved at 3.3 wt.% in a 1:1 wt/wt mixture of chlorobenzene (CB) and dichlorobenzene (DCB) (anhydrous, purchased from Sigma–Aldrich) and stirred overnight at 100°C. Substrates comprised 1.1-mm-thick glass of varying dimensions (UV–vis and Raman analysis) and 500-µm-thick undoped, double-sided polished silicon cut to 14 × 14 mm^2 size (SEM analysis). Substrates were cleaned by sequential cleaning with acetone and isopropanol in an ultrasonic bath.

4.2 | PBTTT Film Fabrication

4.2.1 | Blade-Coating Procedure

Blade-coating was performed under ambient atmosphere (Erichsen Coatmaster 510 stage and Zehntner ZUA 2000 applicator) using plate temperature = 65°C and blade height = 300 µm. A USB-powered fan is attached close to the applicator and directed at the substrate to control the film drying kinetics as described in refs [33, 45] and indicated in Figure 1b. PBTTT solution was heated to 125°C for 15 min and subsequently kept at 100°C immediately prior to coating. 55 µL of solution were used for 25 mm substrate width. Coating was performed at a speed of 3 mm s^{-1}, and the fan was turned on simultaneously upon starting the coating process, resulting in ∼160-nm-thick films. Following coating, PBTTT films were crystallized by annealing on a hotplate at 150°C in a nitrogen-filled glove box for 20 min, with subsequent slow cooling to 100°C (confirmation of the enhanced crystallinity can be seen in the UV–vis data provided in Figure S9).

4.2.2 | Vapor-Phase Doping

Doping of PBTTT with F_4TCNQ was performed by adapting the previously described procedure involving controlled elevated PBTTT film temperature (see [30] and the corresponding Supporting Information). Approximately 20 mg of F_4TCNQ powder (Ossila, CAS: 29261-33-4) were spread in a 6.5 cm deep petri dish. The polymer samples attached to upside-down to the lid of the petri dish were then placed on top to form a closed container. A hotplate was heated to 225°C, and a cylindrical block of aluminum with a similar diameter to the petri dish was placed on a second hotplate at 140°C. The Petri dish was then placed on the first hotplate, and the aluminum block is added on top to control PBTTT film temperature. The standard time for doping was 15 min, and the lid containing the PBTTT films was rotated by 90° every 60 s. Vapor phase doping with F_4TCNQ can lead to the formation of surface crystals of neutral dopant, which were thereafter removed by two blade-coating passes with acetonitrile as the optimal solvent for F_4TCNQ (80 µL, speed = 5 mm s^{-1}, blade height = 300 µm). See Figures S10 and S11 for UV–vis measurements and additional info on the influence of acetonitrile on the PBTTT:F_4TCNQ film.

4.3 | Laser Path Control and Laser De-Doping

Laser paths were created via CAD-sketches in the open-source software solution FreeCAD (v0.19). The sketches were exported to G-Code via a custom FreeCAD post-processor based on Python scripts and are used to control the laser systems (positioning and output power). The laser has a positioning accuracy of ±1 µm and is integrated into an industrial-sized Notion Systems n.jet 300 inkjet printing platform. Processing of the polymer thin films was done in the focal spot of the laser. Laser patterning of areas was performed by utilizing raster scans of overlapping adjacent laser swaths with an interline laser swath spacing d = 6 µm, unless specifically stated otherwise. The focused laser has a theoretical, calculated beam diameter of 12.2 µm for 561 nm and 15.3 µm for 785 nm excitation, see also Table S1 and Equation (1). The laser system operating at 785 nm is an Omicron LuxX cw-diode laser. The laser at 561 nm is a Coherent OBIS LX cw-diode laser. Both systems are integrated into a LightHUB Laser Combiner by Omicron Laserage Laserprodukte GmbH.

4.4 | Characterization Methods

UV–vis measurements were performed to record absorption spectra in the 200–1100 nm spectral range using a custom-built setup comprising an AvaLight-DHS-Bal light source and AvaSpec-ULS3648 spectrometer (no correction for scattering or reflection losses).

Electrical resistance of polymer films was measured using a four-point probe station (302 Resistivity Stand with SP4 probe head, Lucas Signatone Corp.) connected to a Keithley 2400 source measurement unit (SMU). After contact of the probe head with the PBTTT thin film, an idle waiting time of t = 60 s happened before the measurement value was recorded.

Spectroscopic Raman and photoluminescence (PL) mapping were performed using a WITec Alpha 300RA+ instrument equipped with a 100× objective using excitation at 488 (Raman) and 532 nm (PL). Measurements were performed for 50 × 50 $µm^2$ areas in scanning mode. Laser power and integration time were optimized to minimize any simultaneous sample de-doping during imaging. Polynomial backgrounds were subtracted from the spectra using the WITec Project Five software.

2365709x, 0, Downloaded from https://advanced.onlinelibrary.wiley.com/doi/10.1002/admt.71298, Wiley Online Library on [14/09/2026]. See the Terms and Conditions (https://onlinelibrary.wiley.com/terms-and-conditions) on Wiley Online Library for rules of use; OA articles are governed by the applicable Creative Commons License

Acknowledgements

This work was funded by the Deutsche Forschungsgemeinschaft (DFG, German Research Foundation) under Germany's Excellence Strategy for funding via the Excellence Cluster "3D Matter Made to Order" (EXC-2082/2-390761711). G.H.S. thanks DFG (Heisenbergprofessur, HE 7056/7-1) for the financial support. A.P. acknowledges the financial support by the Federal Ministry of Education and Research (BMBF) and the Baden-Württemberg Ministry of Science as part of the Excellence Strategy of the German Federal and State Governments. C.R. acknowledges support by the Karlsruhe School of Optics & Photonics (KSOP) and the Ministry of Science, Research and Arts of Baden-Württemberg as part of the sustainability financing of the projects of the Excellence Initiative II. The authors further thank Prof. Mariano Campoy-Quiles (ICMAB-CSIC) for providing access to the Raman mapping equipment, as well as freely-shared insights into spectroscopic analysis of doped molecular semiconductors.

Open access funding enabled and organized by Projekt DEAL.

Conflicts of Interest

The authors declare no conflicts of interest.

Data Availability Statement

The data that support the findings of this study are available from the corresponding author upon reasonable request.

References

1. A. D. Scaccabarozzi, A. Basu, F. Aniés, et al., "Doping Approaches for Organic Semiconductors," *Chemical Reviews* 122, no. 4 (2022): 4420–4492, https://doi.org/10.1021/acs.chemrev.1c00581.

2. B. Lüssem, M. Riede, and K. Leo, "Doping of Organic Semiconductors," *Physica Status Solidi (a)* 210, no. 1 (2013): 9–43.

3. T. H. Kim, J. H. Kim, and K. Kang, "Molecular Doping Principles in Organic Electronics: Fundamentals and Recent Progress," *Japanese Journal of Applied Physics* 62, no. SE (2023): SE0803, https://doi.org/10.35848/1347-4065/acbb10.

4. K. Pei, "Recent Advances in Molecular Doping of Organic Semiconductors," *Surfaces and Interfaces* 30 (2022): 101887, https://doi.org/10.1016/j.surfin.2022.101887.

5. I. E. Jacobs and A. J. Moulé, "Controlling Molecular Doping in Organic Semiconductors," *Advanced Materials* 29, no. 42 (2017): 1–39, https://doi.org/10.1002/adma.201703063.

6. M. Pfeiffer, K. Leo, X. Zhou, et al., "Doped Organic Semiconductors: Physics and Application in Light Emitting Diodes," *Organic Electronics* 4, no. 2–3 (2003): 89–103, https://doi.org/10.1016/j.orgel.2003.08.004.

7. K. T. Kamtekar, A. P. Monkman, and M. R. Bryce, "Recent Advances in White Organic Light-Emitting Materials and Devices (WOLEDs)," *Advanced Materials* 22, no. 5 (2010): 572–582, https://doi.org/10.1002/adma.200902148.

8. T. Schneider, S. Gärtner, B. Ebenhoch, J. Behrends, and A. Colsmann, "Enhanced Electron Extraction From Solution Processed Organic Solar Cells Employing Rhodamine B Doped Fullerene Layers," *Synthetic Metals* 221 (2016): 201–205, https://doi.org/10.1016/j.synthmet.2016.09.003.

9. F. Manger, P. Marlow, K. Fischer, M. Nöller, C. Sprau, and A. Colsmann, "Organic Solar Cells: Electrostatic Stabilization of Organic Semiconductor Nanoparticle Dispersions by Electrical Doping," *Advanced Functional Materials* 32, no. 33 (2022): 1–10, https://doi.org/10.1002/adfm.202202566.

10. Y. Xu, H. Sun, A. Liu, et al., "Doping: A Key Enabler for Organic Transistors," *Advanced Materials* 30, no. 46 (2018): 13–19, https://doi.org/10.1002/adma.201801830.

11. D. E. Kim and K. J. Baeg, "Reduction Treatment of Molecular-Doped Polymer Semiconductors for High-Performance N-Channel Organic Field-Effect Transistors," *Journal of the Korean Physical Society* 75, no. 10 (2019): 821–826, https://doi.org/10.3938/jkps.75.821.

12. C. H. Wang, X. Gao, Y. N. Zhong, J. Liu, J. L. Xu, and S. D. Wang, "Controlled Surface Doping for Operating Stability Enhancement in Organic Field-effect Transistors," *Organic Electronics* 42 (2017): 367–371, https://doi.org/10.1016/j.orgel.2016.12.051.

13. S. P. Tiwari, W. J. Potscavage, T. Sajoto, S. Barlow, S. R. Marder, and B. Kippelen, "Pentacene Organic Field-effect Transistors With Doped Electrode-semiconductor Contacts," *Organic Electronics* 11, no. 5 (2010): 860–863, https://doi.org/10.1016/j.orgel.2010.01.029.

14. T. Ma, W. Kent, B. X. Dong, G. L. Grocke, and S. N. Patel, "Continuously Graded Doped Semiconducting Polymers Enhance Thermoelectric Cooling," *Applied Physics Letters* 119, no. 1 (2021): 013902, https://doi.org/10.1063/5.0055634.

15. O. Zapata-Arteaga, A. Perevedentsev, S. Marina, J. Martin, J. S. Reparaz, and M. Campoy-Quiles, "Reduction of the Lattice Thermal Conductivity of Polymer Semiconductors by Molecular Doping," *ACS Energy Letters* 5, no. 9 (2020): 2972–2978, https://doi.org/10.1021/acsenergylett.0c01410.

16. Y. Zhang, B. De Boer, and P. W. M. Blom, "Controllable Molecular Doping and Charge Transport in Solution-Processed Polymer Semiconducting Layers," *Advanced Functional Materials* 19, no. 12 (2009): 1901–1905, https://doi.org/10.1002/adfm.200801761.

17. K.-H. Yim, G. L. Whiting, C. E. Murphy, et al., "Controlling Electrical Properties of Conjugated Polymers via a Solution-Based p-Type Doping," *Advanced Materials* 20, no. 17 (2008): 3319–3324, https://doi.org/10.1002/adma.200800735.

18. P. Pingel and D. Neher, "Comprehensive Picture of *p*-type Doping of P3HT With the Molecular Acceptor F_4TCNQ," *Physical Review B—Condensed Matter and Materials Physics* 87, no. 11 (2013): 1–9, https://doi.org/10.1103/PhysRevB.87.115209.

19. E. F. Aziz, A. Vollmer, S. Eisebitt, et al., "Localized Charge Transfer in a Molecularly Doped Conducting Polymer," *Advanced Materials* (2007): 3257–3260, https://doi.org/10.1002/adma.200700926.

20. M. T. Fontana, D. A. Stanfield, D. T. Scholes, K. J. Winchell, S. H. Tolbert, and B. J. Schwartz, "Evaporation vs Solution Sequential Doping of Conjugated Polymers: F_4TCNQ Doping of Micrometer-Thick P3HT Films for Thermoelectrics," *The Journal of Physical Chemistry C* 123, no. 37 (2019): 22711–22724, https://doi.org/10.1021/acs.jpcc.9b05069.

21. T. Ma, B. X. Dong, G. L. Grocke, J. Strzalka, and S. N. Patel, "Leveraging Sequential Doping of Semiconducting Polymers to Enable Functionally Graded Materials for Organic Thermoelectrics," *Macromolecules* 53, no. 8 (2020): 2882–2892, https://doi.org/10.1021/acs.macromol.0c00402.

22. Y. Kim, K. Broch, W. Lee, et al., "Highly Stable Contact Doping in Organic Field Effect Transistors by Dopant-Blockade Method," *Advanced Functional Materials* 30, no. 28 (2020): 2000058, https://doi.org/10.1002/adfm.202000058.

23. J. Zhang, B. Geng, S. Duan, et al., "High-resolution Organic Field-Effect Transistors Manufactured by Electrohydrodynamic Inkjet Printing of Doped Electrodes," *Journal of Materials Chemistry C* 8, no. 43 (2020): 15219–15223, https://doi.org/10.1039/d0tc02508a.

24. J. Fuzell, I. E. Jacobs, S. Ackling, et al., "Optical Dedoping Mechanism for P3HT:F4TCNQ Mixtures," *The Journal of Physical Chemistry Letters* 7, no. 21 (2016): 4297–4303, https://doi.org/10.1021/acs.jpclett.6b02048.

25. I. E. Jacobs, E. W. Aasen, D. Nowak, et al., "Direct-Write Optical Patterning of P3HT Films Beyond the Diffraction Limit," *Advanced Materials* 29, no. 2 (2017): 1603221, https://doi.org/10.1002/adma.201603221.

26. I. E. Jacobs, J. Li, S. L. Burg, et al., "Reversible Optical Control of Conjugated Polymer Solubility With Sub-Micrometer Resolution," *ACS Nano* 9, no. 2 (2015): 1905–1912.

2365709x, 0, Downloaded from https://advanced.onlinelibrary.wiley.com/doi/10.1002/admt.71298, Wiley Online Library on [14/09/2026]. See the Terms and Conditions (https://onlinelibrary.wiley.com/terms-and-conditions) on Wiley Online Library for rules of use; OA articles are governed by the applicable Creative Commons License

27. A. Perevedentsev and M. Campoy-Quiles, "Rapid and High-Resolution Patterning of Microstructure and Composition in Organic Semiconductors Using 'Molecular Gates'," *Nature Communications* 11, no. 2020 (2020): 3610, https://doi.org/10.1038/s41467-020-17361-8.

28. O. Zapata-Arteaga, A. Perevedentsev, M. Prete, et al., "A Universal, Highly Stable Dopant System for Organic Semiconductors Based on Lewis-Paired Dopant Complexes," *ACS Energy Letters* 9 (2024): 3567–3577, https://doi.org/10.1021/acsenergylett.4c01278.

29. J. E. Cochran, M. J. N. Junk, A. M. Glaudell, et al., "Molecular Interactions and Ordering in Electrically Doped Polymers: Blends of PBTTT and F_4TCNQ," *Macromolecules* 47, no. 19 (2014): 6836–6846, https://doi.org/10.1021/ma501547h.

30. O. Zapata-Arteaga, B. Dörling, A. Perevedentsev, J. Martín, J. S. Reparaz, and M. Campoy-Quiles, "Closing the Stability–Performance Gap in Organic Thermoelectrics by Adjusting the Partial to Integer Charge Transfer Ratio," *Macromolecules* 53, no. 2 (2020): 609–620, https://doi.org/10.1021/acs.macromol.9b02263.

31. V. Vijayakumar, P. Durand, H. Zeng, et al., "Influence of Dopant Size and Doping Method on the Structure and Thermoelectric Properties of PBTTT Films Doped With F_6TCNNQ and F_4TCNQ," *Journal of Materials Chemistry C* 8, no. 46 (2020): 16470–16482, https://doi.org/10.1039/d0tc02828b.

32. S. N. Patel, A. M. Glaudell, K. A. Peterson, et al., "Morphology Controls the Thermoelectric Power Factor of a Doped Semiconducting Polymer," *Science Advances* 3 (2017): 24–26.

33. H. Mejri, A. Haidisch, P. Krebsbach, M. Seiberlich, G. Hernandez-Sosa, and A. Perevedentsev, "Gas-Assisted Blade-Coating of Organic Semiconductors: Molecular Assembly, Device Fabrication and Complex Thin-film Structuring," *Nanoscale* 14, no. 47 (2022): 17743–17753, https://doi.org/10.1039/d2nr05947a.

34. K. Kang, S. Watanabe, K. Broch, et al., "2D Coherent Charge Transport in Highly Ordered Conducting Polymers Doped by Solid State Diffusion," *Nature Materials* 15, no. 8 (2016): 896–902, https://doi.org/10.1038/nmat4634.

35. J. Li, C. Koshnick, S. O. Diallo, et al., "Quantitative Measurements of the Temperature-Dependent Microscopic and Macroscopic Dynamics of a Molecular Dopant in a Conjugated Polymer," *Macromolecules* 50 (2017): 5476–5489, https://doi.org/10.1021/acs.macromol.7b00672.

36. J. Li, D. M. Holm, S. Guda, and Z. I. Bedolla-valdez, "Effect of Processing Conditions on Additive DISC Patterning of P3HT Films," *Journal of Materials Chemistry C* 7 , no. 2018 (2019): 302–313, https://doi.org/10.1039/C8TC04519D.

37. L. Müller, S.-Y. Rhim, V. Sivanesan, et al., "Electric-Field-Controlled Dopant Distribution in Organic Semiconductors," *Advanced Materials* 29, no. 30 (2017): 1–7, https://doi.org/10.1002/adma.201701466.

38. J. Li, C. W. Rochester, I. E. Jacobs, et al., "The Effect of Thermal Annealing on Dopant Site Choice in Conjugated Polymers," *Organic Electronics* 33 (2016): 23–31, https://doi.org/10.1016/j.orgel.2016.02.029.

39. A. Rodrigues, M. C. R. Castro, A. S. F. Farinha, et al., "Thermal Stability of P3HT and P3HT:PCBM Blends in the Molten state," *Polymer Testing* 32, no. 7 (2013): 1192–1201, https://doi.org/10.1016/j.polymertesting.2013.07.008.

40. R. Ramani, J. Srivastava, and S. Alam, "Application of Model-free Kinetics to the Thermal and Thermo-Oxidative Degradation of Poly(3-hexyl thiophene)," *Thermochimica Acta* 499, no. 1–2 (2010): 34–39, https://doi.org/10.1016/j.tca.2009.10.019.

41. V. Pirela, A. J. Müller, and J. Martín, "Crystallization Kinetics of Semiconducting poly(2,5-bis(3-Alkylthiophen-2-Yl)-Thieno-[3,2-B]thiophene) (PBTTT) From Its Different Liquid Phases," *Journal of Materials Chemistry C* 12, no. 11 (2024): 4005–4012, https://doi.org/10.1039/d3tc03850e.

42. S. Kim, M. A. M. Rashid, T. Ko, et al., "New Insights Into the Photodegradation Mechanism of the PTB7-Th Film: Photooxidation of π-Conjugated Backbone Upon Sunlight Illumination," *The Journal of Physical Chemistry C* 124 (2020): 2762–2770, https://doi.org/10.1021/acs.jpcc.9b09954.

43. C. Francis, D. Fazzi, S. B. Grimm, et al., "Raman Spectroscopy and Microscopy of Electrochemically and Chemically Doped High-Mobility Semiconducting Polymers," *Journal of Materials Chemistry C* 5 (2017): 6176–6184, https://doi.org/10.1039/C7TC01277B.

44. J. Panidi, A. F. Paterson, D. Khim, et al., "Remarkable Enhancement of the Hole Mobility in Several Organic Small-Molecules, Polymers, and Small-Molecule:Polymer Blend Transistors by Simple Admixing of the Lewis Acid p-Dopant $B(C_6F_5)_3$," *Advanced Science* 5, no. 1 (2018): 1700290, https://doi.org/10.1002/advs.201700290.

45. A. Perevedentsev, H. Mejri, L. A. Ruiz-Preciado, et al., "Polarization-Sensitive Photodetectors Based on Directionally Oriented Organic Bulk-Heterojunctions," *Advanced Optical Materials* 10, no. 7 (2022): 2102397, https://doi.org/10.1002/adom.202102397.

Supporting Information

Additional supporting information can be found online in the Supporting Information section.

Supporting File: admt71298-sup-0001-SuppMat.docx.

2365709x, 0, Downloaded from https://advanced.onlinelibrary.wiley.com/doi/10.1002/admt.71298, Wiley Online Library on [14/09/2026]. See the Terms and Conditions (https://onlinelibrary.wiley.com/terms-and-conditions) on Wiley Online Library for rules of use; OA articles are governed by the applicable Creative Commons License